applied sciences

MDPI

Article

Design and Performance Analysis of a Micro-Axial Compressor for Downhole Boosting

Jianyi Liu and Jiali Zhu *

National Key Laboratory of Oil and Gas Reservoir Geology and Exploration, Southwest Petroleum University, Chengdu 610500, China; liujianyi163@163.com
* Correspondence: 18306044128@163.com

Abstract

Downhole boosting technology breaks the physical limitations of conventional surface boosting by enhancing pressure at the wellbore bottom, with micro-axial compressors serving as its core compression module. However, traditional axial compressors, when miniaturized, suffer from severe end losses and easy instability, failing to adapt to downhole space constraints and the efficient pressurization demands of low-permeability, low-pressure, and small-flow reservoirs. To address this, this study designed a compact micro-axial compressor. CFturbo was used for parametric blade design and optimization, while ANSYS CFX 2025 (with the SST turbulence model) conducted numerical simulations. A "simulation–diagnosis–optimization–validation" closed-loop strategy was adopted to adjust the blade's leading-edge shape, camber line, and thickness distribution, combined with grid independence verification and inter-stage matching optimization. The results show that at the design speed (60,000 rpm), the compressor achieves a pressure ratio of 1.57 and an isentropic efficiency of 83.6%. It also maintains stable performance at 55,000 rpm (off-design speed), with excellent inter-stage aerodynamic matching and controllable leakage losses. This compressor meets downhole operational needs, providing technical support for developing low-permeability, low-pressure, small-flow reservoirs.

Keywords: micro-axial compressor; downhole boosting; blade optimization; numerical simulation; aerodynamic performance; low-flow reservoir

1. Introduction

In recent years, research and field trials have shown that placing compressors inside wellbores near reservoirs yields economic benefits surpassing those of conventional surface boosting technologies. As the core module of downhole boosting systems, axial compressors exhibit excellent adaptability to harsh downhole environments, featuring a wide operating range, strong compatibility with complex fluids, and high energy conversion efficiency. Such advantages make them a critical component for addressing the challenges of low-permeability, low-pressure, and small-flow rate reservoir development.

Axial compressors have long dominated high-flow, high-power application scenarios—including aircraft engines, large gas turbines, and wind tunnels—due to their robust flow-handling capacity, moderate single-stage pressure ratio, high efficiency, and compact axial dimensions [1]. However, traditional axial compressors face inherent limitations when scaled down for micro-applications and ultra-low flow rate conditions: their relatively low stage loading, significantly increased end losses from short blades, and high sensitivity to flow fluctuations (which easily trigger rotating stall and surge) restrict

Check for updates

Received: 19 March 2026
Revised: 22 April 2026
Accepted: 25 April 2026
Published: 28 April 2026

Copyright: © 2026 by the authors. Licensee MDPI, Basel, Switzerland. This article is an open access article distributed under the terms and conditions of the Creative Commons Attribution (CC BY) license.

their performance [2]. With the growing demand for efficient, compact, and adaptable pressurization equipment in emerging fields such as downhole boosting, micro-power systems, and precision environmental control, developing micro-axial compressors tailored to confined spaces (e.g., wellbores) and low-permeability, small-flow reservoirs has become a key technical trend for enhancing overall system performance.

Existing research on micro-axial compressors has primarily focused on aircraft engines and ground-based gas turbines, with limited attention to structural and aerodynamic designs adapted to wellbore environments. Liao et al. proposed an integral design theory for small high-pressure fans, simplifying the radial equilibrium equation via Taylor expansion and integrating a diffusion factor loss model with blade height/clearance corrections [3]. Experimental validation showed that the design achieved a pressure of 4480 Pa (exceeding the target by 28%) and an efficiency of 78%, close to predicted values; this provides a foundational framework for the parametric design of micro-compressors in this study (referenced in Section 2.1 for initial blade parameter setting). Guo et al. optimized stator aerodynamic performance by adjusting flow path curvature: changing the tip flow path from inclined to horizontal reduced the root peak Mach number by 13.8%, while a downstream trailing edge expansion design weakened radial flow, making the surface Mach number distribution approximate to that of a controlled diffusion airfoil (uniformity improved by 20%) [4]. This optimization strategy informed the stator flow path modification in our blade optimization process (referenced in Section 3.2 for first-stage stator camber line adjustment).

Song et al. was used to observe spanwise non-uniformity in stator wakes, finding that turbulence intensity at the root and tip was 15% higher than in the mainstream; when the flow rate dropped to a critical value, the root region became fully low-speed, turbulence intensity surged by 80%, and the wake center shifted by 4.3% pitch toward the suction side [5]. This insight guided our analysis of flow separation mechanisms in the initial compressor model (referenced in Section 3.2 for diagnosing root low-speed regions in rotor/stator flow fields). Staedter et al. achieved breakthroughs in micro-turbojet engine performance through full 3D optimization of compressors (enhancing mid-span to tip loading) and turbines (load factor 0.309), resulting in an average compressor stage pressure ratio of 1.64 [6]. This load distribution optimization method was adapted for our multi-stage compressor blade loading adjustment (referenced in Section 3.1 for determining optimization priorities of mid-span to tip regions).

Wu S et al. optimized the inter-stage load distribution of a five-stage compressor based on the Smith chart (high loading in middle stages and low loading in the first and last stages), achieving a design point efficiency of 0.871 and a margin of 26.2% [7]. Their inter-stage matching strategy is referenced in Section 3.4 to verify the three-stage rotor–stator aerodynamic coordination of our compressor. He et al. used Kulite sensors and high-frequency probes to reveal the rotational speed dependence of inter-stage interference in small-scale compressors: at high speeds, interference was limited to the first-stage rotor trailing edge (superimposed frequency amplitude <5% fundamental frequency), while at medium and low speeds, interference extended to the leading edge. This finding was cited in Section 3.3 to explain the slight pressure ratio fluctuation at 55,000 rpm (off-design speed) [8].

Neumeier et al. used parametric modeling (Workbench) to identify the U-shaped curve law of circumferential dovetail tenon stress, deriving the quadratic function $\sigma = 0.1dsh^2 - 3.2dsh + 160$ ($R^2 > 0.94$) for average working surface stress [9]. This structural stress calculation method is referenced in Section 2.1 to ensure the mechanical stability of our compressor's blade-tenon connection.

Grieb et al. used the nonlinear harmonic method to study tip clearance flow in multi-stage axial compressors, identifying an optimal clearance that maximizes stall margin [10].

This is referenced in Section 3.5 to explain the stable pressure ratio maintenance of our compressor under different flow rates.

Zhao et al. conducted thermodynamic and dynamic investigations of ultra-high-pressure diaphragm compressors, providing insights into high-pressure compression mechanisms that supported our selection of methane as the simulation medium (referenced in Section 2.2 for confirming the compressible fluid property settings) [11]. Yang et al. combined numerical simulation and experimental research to analyze the thermodynamic characteristics of hyper-compressors; their experimental validation method is referenced in Section 3.3 to design the performance test scheme for our optimized compressor [12]. Gao et al. proposed a self-air-cooling reciprocating compressor design; while our study focuses on axial compressors, their thermal management analysis is referenced in Section 2.2 to justify the 364 K downhole temperature setting [13].

Rusanov studied the thermodynamic features of metal hydride thermal sorption compressors, providing a comparative reference for our analysis of axial compressor energy conversion efficiency (referenced in Section 3.5 for evaluating isentropic efficiency advantages) [14]. Li et al. developed an ejector-based detection system for compressor thermodynamic measurement; their performance testing methodology is referenced in Section 3.3 to establish the pressure ratio-mass flow test protocol [15]. Li et al. analyzed the thermodynamic performance of linear compressors using R1234yf, offering a framework for our refrigerant (methane) thermodynamic property calculation (referenced in Section 2.3 for setting SST turbulence model parameters) [16].

Zhao et al. applied a fluid–structure interaction model to analyze boil-off gas compressors, highlighting the importance of multi-physical field coupling: this is referenced in Section 3.4 to explain the streamline evolution mechanism during compressor startup [17]. Sharma et al. conducted thermodynamic analysis of two-stage metal hydride hydrogen compressors, providing a multi-stage compression efficiency comparison benchmark (referenced in Section 3.3 for evaluating the three-stage pressure ratio advantage of our design) [18]. Ma et al. studied the impact of surface roughness on axial compressor blade performance under different altitudes: this is referenced in Section 2.1 to set the blade surface roughness coefficient in our 3D model [19].

Zhang et al. numerically found that increasing hub clearance reduces compressor efficiency but improves flow stability, while expanding and shrinking non-uniform clearances have opposite effects on compressor loss, unsteady flow and stall characteristics [20]. Pinelli studied forced response in multi-stage aeroderivative axial compressors, providing a basis for our unsteady flow characteristic analysis (referenced in Section 3.4 for interpreting the 59th-order mode excitation at medium speeds) [21].

Cai et al. designed passive magnetic mechanisms for axial gas force balance in miniature scroll compressors: their force balance design concept is referenced in Section 2.1 to ensure the rotor's dynamic balance in our micro-compressor [22]. Li et al. coupled a stability-enhancing mechanism with self-recirculating injection in axial compressors: this stability control method is referenced in Section 3.5 to explain our compressor's wide stable operating range [23]. Yokoyama simulated flow and sound around small axial fans with casing slits: their computational domain setting method is referenced in Section 2.3 to define our compressor's inlet/outlet boundary conditions [24].

Kim corrected a one-dimensional axial compressor model using measurement data: this model correction approach is referenced in Section 3.3 to calibrate our numerical simulation results against theoretical pressure ratio calculations [25].

As the core module of downhole boosting equipment, the flow path and blade design of micro-axial compressors directly determine their overall performance. To address the technical gaps in wellbore-adapted designs, this paper proposes a micro-axial

compressor structure tailored for downhole boosting. Blade parameterization is used for design selection, combined with CFturbo for real-time optimization and CFX for performance comparison and validation, aiming to develop a high-efficiency, compact micro-axial compressor suitable for low-permeability, low-pressure, and small-flow rate downhole conditions.

In summary, while prior studies have advanced axial compressor design for aerospace and ground-based applications, limited attention has been paid to micro-scale compressors tailored for downhole boosting. The unique constraints of wellbore environments—tight radial space, low-flow pressurization demands, and variable downhole conditions—remain unaddressed in the existing literature. This work bridges this gap by proposing a compact three-stage micro-axial compressor specifically designed for downhole installation, employing a flow-diagnosis-driven optimization method to enhance aerodynamic performance under realistic wellbore conditions.

2. Model Design and Establishment

2.1. Model Establishment

The 3D model of the micro-axial compressor in this paper was primarily constructed using CFturbo software (ANSYS 2025). The process for designing the compressor impeller in CFturbo is a systematic iterative process. Based on the target pressure ratio (1.5), the key dimensions of the impeller inlet and outlet were preliminarily determined, while strictly limiting the maximum external dimensions of the compressor within the outer diameter of the tubing to meet downhole installation space constraints. Within these dimensional boundaries, a smoothly transitioning meridional flow path contour was constructed by adjusting the hub and shroud profiles to optimize the fluid expansion path. The blade profiling stage focused on defining the circumferential and radial distribution of blade angles, determining the number of blades, and generating a camber surface with specific 3D twist and thickness distribution. The initial model had a maximum outer diameter of 77 mm and consisted of three rotor–stator stages. Details of the structure are illustrated in Table 1 and Figure 1, exclusive of the casing. The entire parametric design process allows for real-time model generation and rapid performance estimation, supporting multiple rounds of iterative optimization of geometric parameters until aerodynamic performance meets expectations while satisfying spatial constraints.

Table 1. Design parameters of the three-stage axial compressor.

Stage		Mean Chord Length (mm)	Number of Blades	Mean Hub Diameter (mm)
1	Rotor	12	27	44.6
	Stator	13	29	54.5
2	Rotor	10	29	60.1
	Stator	7	31	62.6
3	Rotor	6	35	64.8
	Stator	7.5	37	66



Figure 1. Initial 3D model of the axial compressor.

2.2. Simulation Working Parameters

To simulate real compressor placement conditions, some pre-processing was performed. Nodal analysis of a 3700 m-deep gas well was conducted using Pipesim (2023) software, The wellbore model is shown in Figure 2. As the device is placed near the bottom of the well, a depth of 3450 m (50 m from the tubing bottom) was selected. At this depth, the temperature is 364 K and the pressure is 1.33 MPa. The gaseous medium used in the simulation is methane (compressible).

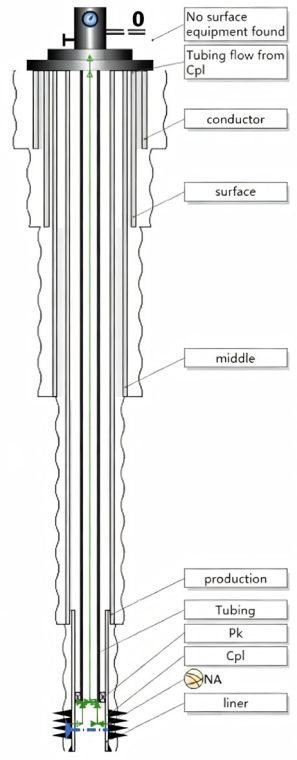


Figure 2. Wellbore model diagram.

2.3. Numerical Method and Boundary Conditions

Flow field simulations were conducted using ANSYS CFX with a pressure-based steady and transient solver. For transient turbomachinery computations, 720 time steps per

revolution were applied (0.5° per step), and temporal independence was verified to ensure time convergence. Blade-passing frequency (BPF) is defined as follows:

$$BPF = Z \times f_r$$

where Z is the number of blades, and f_r is the shaft rotational frequency.

For the first rotor, $BPF = 11 \times 1000 = 11{,}000$ Hz. At least 12 samples per BPF period were stored to guarantee sufficient unsteady resolution. The continuity, momentum, and energy equations and SST turbulence model transport equations are provided below. Standard wall functions were adopted with $30 < y+ < 300$ and no-slip walls. Inlet total pressure = 1.33 MPa, total temperature = 365 K, and outlet average static pressure were applied. The COUPLED algorithm and PRESTO scheme were used. Convergence was achieved when all residuals fell below 10^{-4}.

Flow field analysis of the axial compressor was performed using the ANSYS CFX module, employing a pressure-based steady-state solver for the entire process. The SST model accounts for the transport of turbulent shear stresses in the definition of turbulent viscosity, combining the near-wall accuracy of k-ω with the outer region stability of k-ε. It is suitable for various flow regimes, including separated flows, vortices, and complex shear flows, has lower mesh quality requirements, saves time costs, and performs well in scenarios with adverse pressure gradients. Since this simulation involves a compressor pressurization scenario, the SST turbulence model was selected; the governing equations of the SST turbulence model and the continuity equation are presented below.

For the continuity equation (mass conservation), the integral governing equation of mass conservation for compressible fluids is defined as follows:

$$\frac{\partial}{\partial t}\iiint_V \rho dV + \oint_A \rho v \cdot n dA = 0$$

where ρ is the density of the compressible methane working medium, v is the velocity vector of the fluid, V represents the control volume of the flow field, A is the boundary surface of the control volume, n is the unit outward normal vector of the boundary surface, and t is the flow time.

The eddy viscosity is limited by the shear stress transport limiter to improve predictions under adverse pressure gradients.

$$\mu_t = \frac{\rho a_1 k}{\max(a_1\omega,\, SF_2)}$$

where a_1 is the model constant, S is the magnitude of the strain-rate tensor, F_2 is the second blending function (used to restrict the limiter to boundary-layer regions), k is turbulent kinetic energy, and ω is the specific dissipation rate.

The SST model accounts for the transport of turbulent shear stresses in the definition of turbulent viscosity, combining the near-wall accuracy of k-ω with the outer region stability of k-ε. The Turbulent Kinetic Energy (k) Transport Equation is as follows:

$$\frac{\partial(\rho k)}{\partial t} + \frac{\partial(\rho u_j k)}{\partial x_j} = \frac{\partial}{\partial x_j}\left[(\mu + \sigma_k \mu_t)\frac{\partial k}{\partial x_j}\right] + \widetilde{P}_k - \rho\beta^* k\omega$$

The specific dissipation rate ω transport equation is as follows:

$$\frac{\partial(\rho\omega)}{\partial t} + \frac{\partial(\rho u_j \omega)}{\partial x_j} = \frac{\partial}{\partial x_j}\left[(\mu + \sigma_\omega \mu_t)\frac{\partial \omega}{\partial x_j}\right] + P_\omega + 2(1 - F_1)\frac{\rho\sigma_{\omega 2}}{\omega}\frac{\partial k}{\partial x_j}\frac{\partial \omega}{\partial x_j} - \rho\beta\omega^2$$

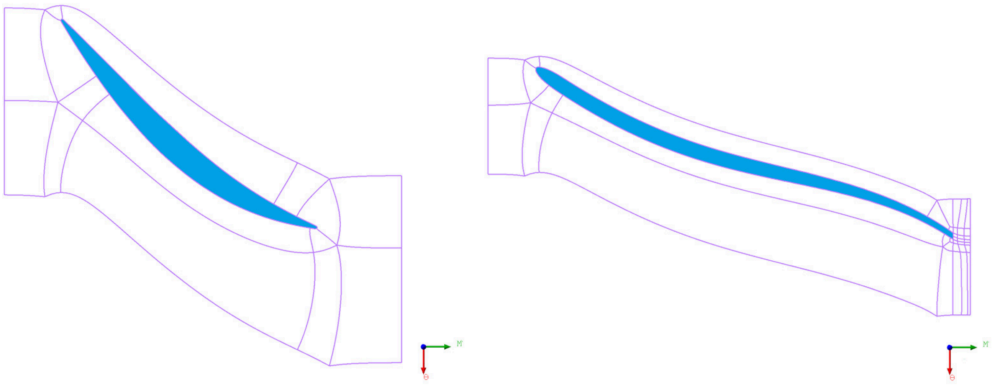
where μ is the dynamic viscosity of the fluid, $\widetilde{P}_k$ is the production term of turbulent kinetic energy, F_1 is the blending function of the SST model, u_j is the velocity component in the x_j direction, x_j is Cartesian coordinate, σ_k is the diffusion Prandtl number for k, β^* is the model constant, and P_w is the production term for ω.

It is suitable for various flow regimes, including separated flows, vortices, and complex shear flows, has lower mesh quality requirements, saves time costs, and performs well in scenarios with adverse pressure gradients. Since this simulation involves a compressor pressurization scenario, the SST turbulence model was selected. Standard wall functions were used for near-wall flow treatment, with no-slip solid walls. The inlet was specified with a total pressure of 1.33 MPa and total temperature of 365 K. The outlet was specified with an average static pressure. The rotor speed was specified. The COUPLED algorithm was used for pressure–velocity coupling. The PRESTO scheme, which is more suitable for rotating machinery, was used for the pressure field. Second-order central difference schemes were used for both the velocity and pressure fields. Relaxation factors were kept at default values. Convergence was considered achieved when residual values fell below 10^{-4}.

2.4. Grid Independence Verification

All simulations were performed on a high-performance computing (HPC) cluster: dual Intel Xeon Gold 6330 CPUs (28 cores per CPU, 2.0 GHz) with 512 GB RAM, and 28-core parallel computing. Each steady simulation took ~3.5 h, and one transient revolution required ~12 h. A zonal meshing strategy was applied: O4H topology inside the blade passage, H-type topology at the inlet/outlet, O-type topology around blade surfaces, and a butterfly grid for tip clearance. Five grid schemes are listed in Table 1. When the grid count exceeded 3.44 million, the pressure ratio and efficiency stabilized, confirming a grid-independent solution. Thus, the 3.44 million grid was adopted.

A core challenge in finite element simulation is grid design: high-resolution grids ensure accuracy but are computationally expensive, while overly simplified grids improve efficiency but may lack fidelity. Therefore, an optimal balance between accuracy and efficiency must be sought. All numerical experiments in this paper were conducted on the ANSYS Workbench (2025) platform, with flow field simulations performed via the CFX module and mesh generation handled by the CFX/Turbo Grid module, specialized for spatial discretization of compressor fluid domains. The single-passage spatial discretization grids for each stage of the axial compressor were generated based on CFX/Turbo Grid. A zonal meshing approach was adopted: OH-type grid topology was used inside the passage, H-type topology at the inlet/outlet, and O-type topology around the blades. A butterfly grid topology was used for the tip clearance, with an inner H-type grid structure surrounded by an O-grid, as seen in Figure 3. The compressor was simulated under an inlet pressure of 1.33 MPa, outlet back pressure of 1.2 MPa, and rotational speed n = 55,000 rpm. Five sets of mesh schemes were designed, as listed in Table 2; the pressure ratio and efficiency trends were obtained for five grid sizes: 2.42 million, 2.85 million, 3.44 million, 4.29 million, and 4.98 million. As is shown in Figure 4, as the number of grid elements increased, both the efficiency and pressure ratio continuously increased until the grid count reached 3.44 million, beyond which the isentropic efficiency and pressure ratio hardly changed. This indicates that further increases in grid count have a negligible impact on the results. Considering computational resources, the 3.44 million grid was selected for the micro-axial compressor calculations. Table 3 presents the mesh quality of the final selected scheme; Figure 5 shows the grid schematic for the third stage of the axial compressor.



(**a**) rotor topology (**b**) stator topology

Figure 3. Third-stage compressor grid schematic.

Table 2. Number of grid elements for different schemes.

Grid Scheme	Rotor	Stator	Total
1	820,499	1,599,503	2,420,002
2	1,030,765	1,820,087	2,850,852
3	1,303,258	2,142,220	3,445,478
4	1,706,580	2,580,903	4,287,483
5	2,091,089	2,890,326	4,981,415

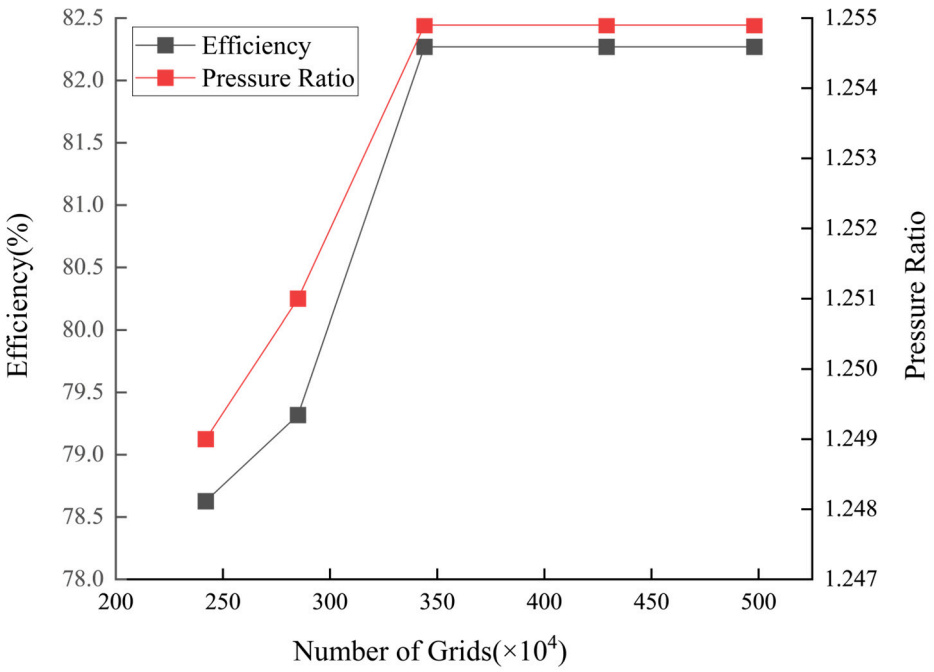
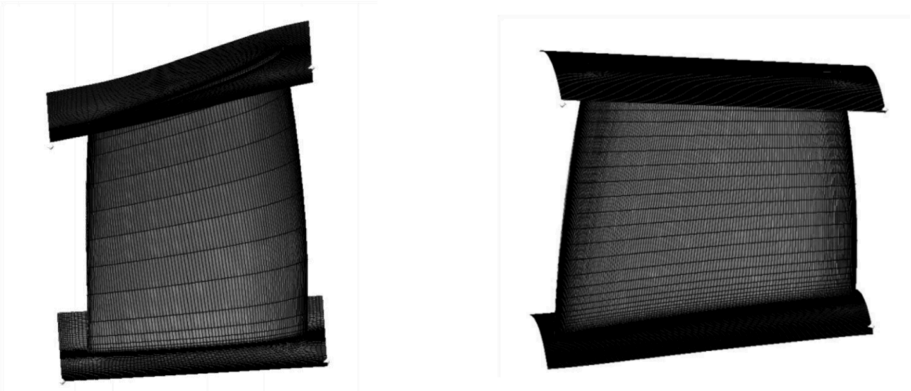


Figure 4. Grid independence verification plot.

Table 3. Mesh statistics.

Stage	Orthog. Angle	Exp. Factor	Aspect Ratio
	Minimum (deg)	Maximum	Maximum
R1	33.2	1.3	245
R2	53.8	1.2	108
R3	21.5	3.3	286
S1	54.5	1.4	299
S2	69.8	1.3	226
S3	54.8	1.3	242



(**a**) Third-stage rotor grid (**b**) Third-stage stator grid

Figure 5. Third-stage compressor grid schematic.

3. Blade Parameter Optimization Based on CFturbo

3.1. Optimization Method and Process Overview

Given the stringent requirements for compressor efficiency and stability in the downhole environment, computationally expensive automated optimization algorithms were abandoned in favor of a problem-oriented sequential optimization method based on flow field diagnostics. A closed-loop process of "simulation–diagnosis–optimization–validation" was adopted. By making geometric adjustments to the blades based on identified flow problems, performance was enhanced.

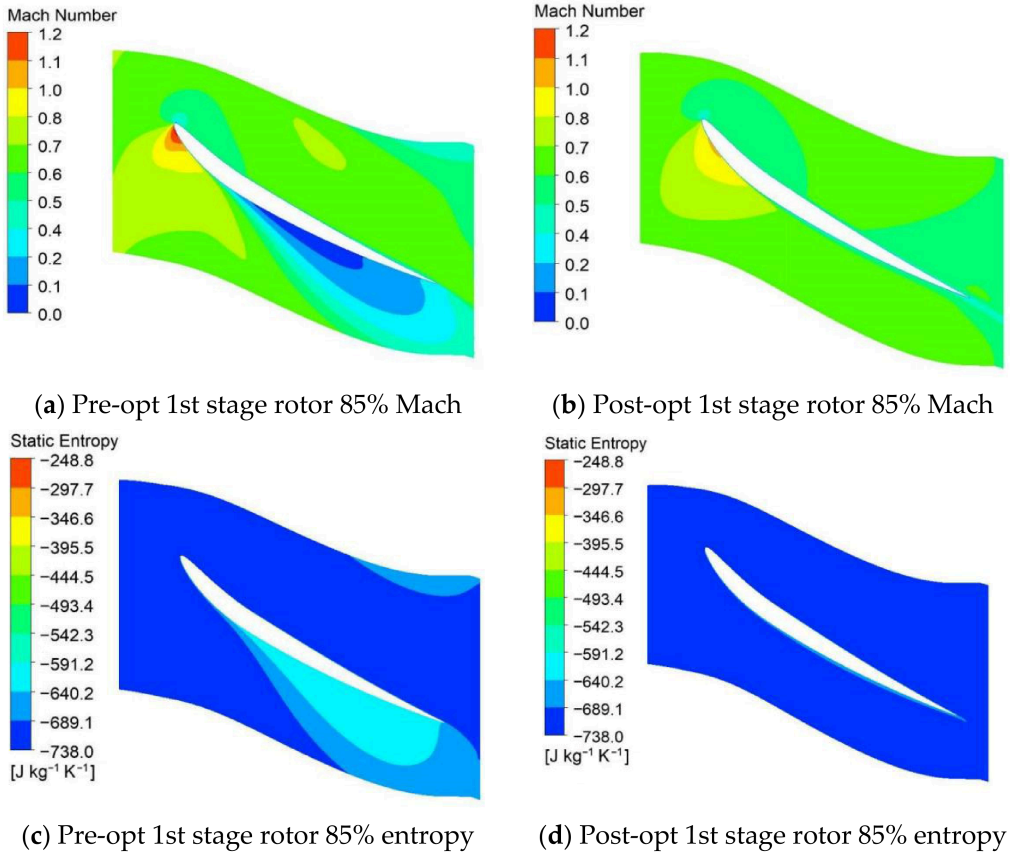
CFD calculations were performed on the initial model to obtain detailed flow field information. Focus was placed on analyzing Mach number and entropy generation contours at the 85% span section to accurately diagnose key issues leading to efficiency loss, such as leading-edge shock and flow separation. Based on the diagnostic results, specific optimization targets were formulated (e.g., "weaken blade leading-edge shock"). Subsequently, relevant geometric parameters (such as blade inlet angle, camber line, and leading-edge shape) were adjusted purposefully in CFturbo to improve the flow structure. The modified model was then re-simulated using CFD, and flow field contours before and after optimization were compared to assess the effectiveness of the measures. Through multiple iterations, the flow problems were significantly improved, and the optimization process converged.

3.2. Internal Flow Field Analysis

This optimization analysis was based on Mach number distribution and entropy generation contours at the 85% span section, conducting multiple rounds of design and numerical simulation in CFturbo. By observing the state of the Mach number and entropy generation contours, targeted adjustments were made to the blades.

From the contour plots Figure 6a,c of the first-stage rotor, it was found that before optimization, there was a significant high-Mach-number shock phenomenon at the leading

edge of the blade suction side, along with obvious flow separation on the suction surface covering a large range, approximately 30% to 100% of the relative chord length. This phenomenon was also reflected in the entropy distribution, showing a large area of high entropy generation on the suction surface. Through continuous adjustment and optimization of the blade structure, this phenomenon was essentially completely eliminated. Specifically, as the shock weakened, the impact intensity of the airflow at the blade leading edge decreased, reducing energy loss. The reduction in the flow separation area stabilized the boundary-layer flow, avoiding vortex losses caused by separation. After multiple iterations, as is shown in Figure 6b, the Mach number distribution at 85% span became more uniform, shock strength was controlled within an acceptable range, overall entropy generation levels decreased, and the blade's aerodynamic performance was significantly improved, laying a good foundation for subsequent stage design. By comparing Figure 6c,d, changes in the entropy generation contours further confirmed the optimization effect: large areas of high entropy generation contracted to localized small regions, indicating smoother airflow over the blade surface and significantly reduced aerodynamic losses.



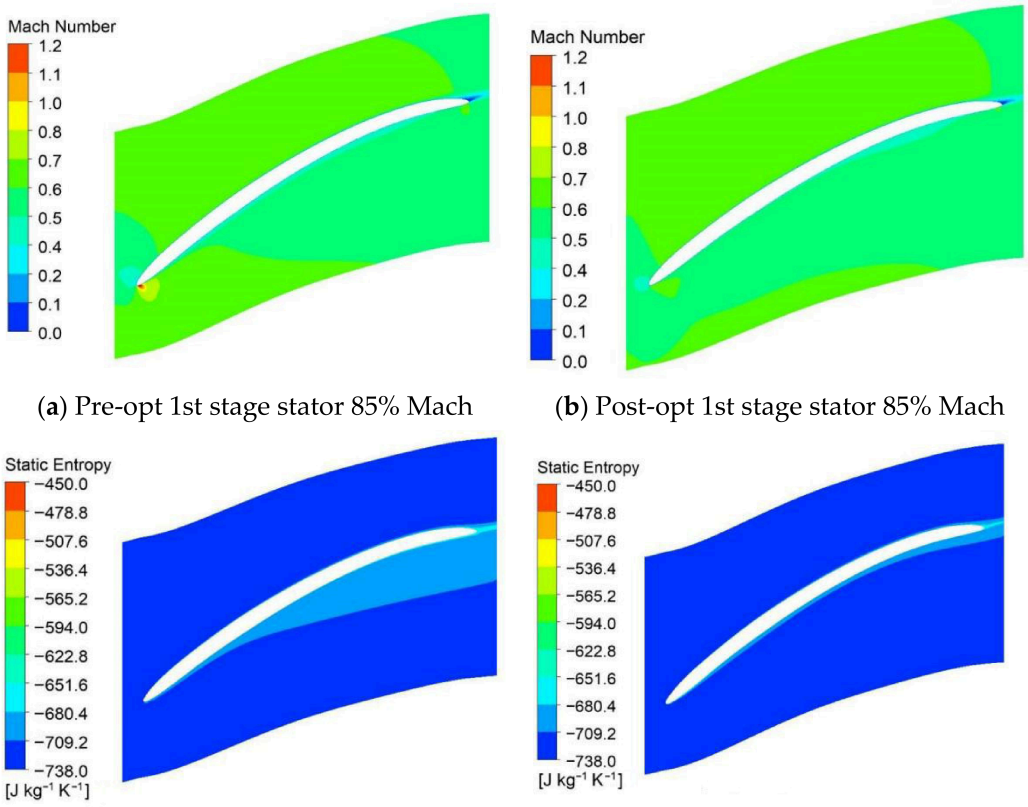
(**a**) Pre-opt 1st stage rotor 85% Mach (**b**) Post-opt 1st stage rotor 85% Mach

(**c**) Pre-opt 1st stage rotor 85% entropy (**d**) Post-opt 1st stage rotor 85% entropy

Figure 6. Comparison of first-stage rotor contours before and after optimization.

In the initial aerodynamic design, as is shown in Figure 7a,c, a distinct high-Mach-number shock structure was observed in the leading-edge region of the first-stage stator, along with significant entropy generation over 30% to 100% of the pressure-side relative chord length, indicating noticeable flow separation and boundary-layer reattachment in this region. This led to increased kinetic energy loss and adversely affected the stability of the downstream rotor flow field. Through targeted aerodynamic optimization, the leading-edge radius was moderately increased to alleviate local acceleration and suppress shock generation, and the camber line configuration and thickness distribution were finely reconstructed, effectively improving the pressure-side flow attachment and reducing

irreversible losses caused by separation. As illustrated in Figure 7b,d, the optimized results showed significantly weakened leading-edge shock strength, more uniform pressure-side velocity distribution, and a clear reduction in the extent and magnitude of the entropy generation region, resulting in a more stable overall flow structure. This optimization not only improved the stator's own aerodynamic efficiency but also significantly enhanced the inlet flow conditions for the downstream rotor, thereby improving the inter-stage aerodynamic matching and energy transfer efficiency, providing effective support for enhancing the overall performance of the multi-stage compressor.

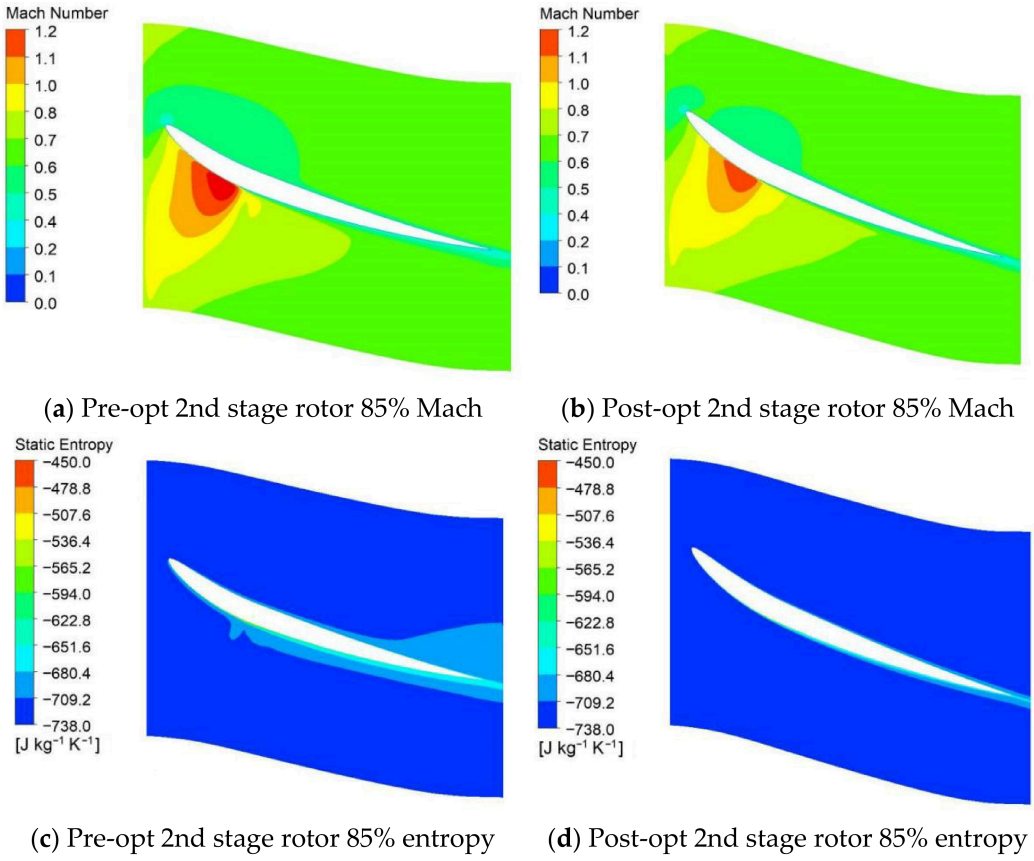


(**a**) Pre-opt 1st stage stator 85% Mach (**b**) Post-opt 1st stage stator 85% Mach

(**c**) Pre-opt 1st stage stator 85% entropy (**d**) Post-opt 1st stage stator 85% entropy

Figure 7. Comparison of first-stage stator contours before and after optimization.

From the Figure 8a,c, it can be observed that in the initial design, the second-stage rotor blade suction side leading edge exhibited a significant high-intensity shock phenomenon, while the entropy distribution indicated some degree of flow separation in both the suction and pressure-side boundary layers. To improve this flow state, the optimization focused on coordinated adjustment of the blade's leading-edge curvature and inlet geometric angle, effectively reducing the shock intensity by decreasing the local flow turning angle at the leading edge and improving the boundary-layer development history. As shown in Figure 8b,d, the optimized flow field results showed that the strong normal shock at the suction-side leading edge transformed into a weak oblique shock system, and shock-induced boundary-layer separation was effectively suppressed, with peak entropy generation reduced compared to before optimization. Simultaneously, the pressure-side boundary-layer velocity gradient decreased significantly, and the accumulation of low-energy fluid in the near-wall region was noticeably alleviated. This optimization effectively eliminated the leading-edge high-Mach-number region and boundary-layer separation, significantly enhancing aerodynamic performance and laying an important foundation for improving the work capacity and anti-stall margin of the downstream rotor.

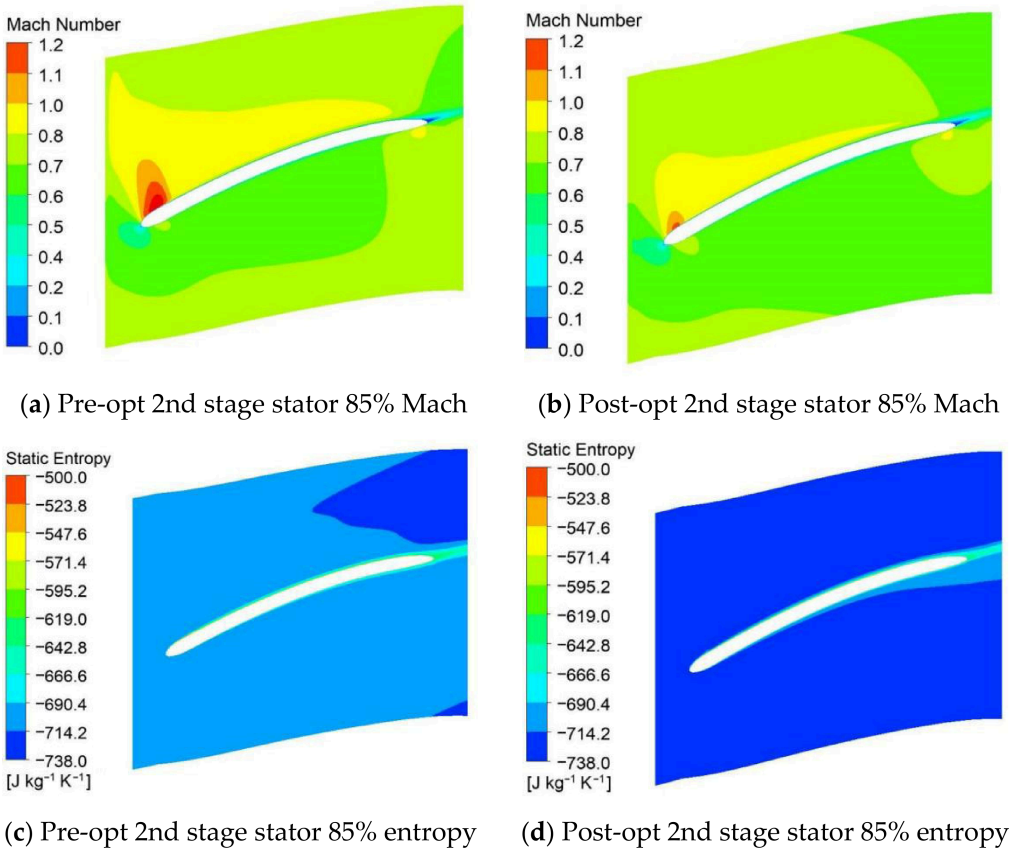


(**a**) Pre-opt 2nd stage rotor 85% Mach (**b**) Post-opt 2nd stage rotor 85% Mach

(**c**) Pre-opt 2nd stage rotor 85% entropy (**d**) Post-opt 2nd stage rotor 85% entropy

Figure 8. Comparison of second-stage rotor contours before and after optimization.

From the Figure 9a,c, it can be seen that a region of high Mach number flow exists at the leading edge of the second-stage stator, indicating the possible presence of a strong local shock. Meanwhile, the entropy generation contours show significant high-entropy regions within the blade passage, reflecting irreversible losses due to flow separation or shock/boundary layer interaction, indicating a relatively disordered flow state. Figure 9b demonstrates that after aerodynamic optimization, the extent of the leading-edge high-Mach-number region was substantially reduced, indicating weakened shock strength or improved shock structure, leading to smoother airflow; Figure 9d demonstrates that the entropy generation within the passage also decreased significantly, indicating reduced flow losses and improved flow characteristics. To further evaluate the optimization effect, a quantitative analysis was performed on the second-stage stator, showing a decrease in the total pressure loss coefficient compared to before optimization, consistent with the observed weakening of the shock structure and reduction in the boundary-layer separation extent.

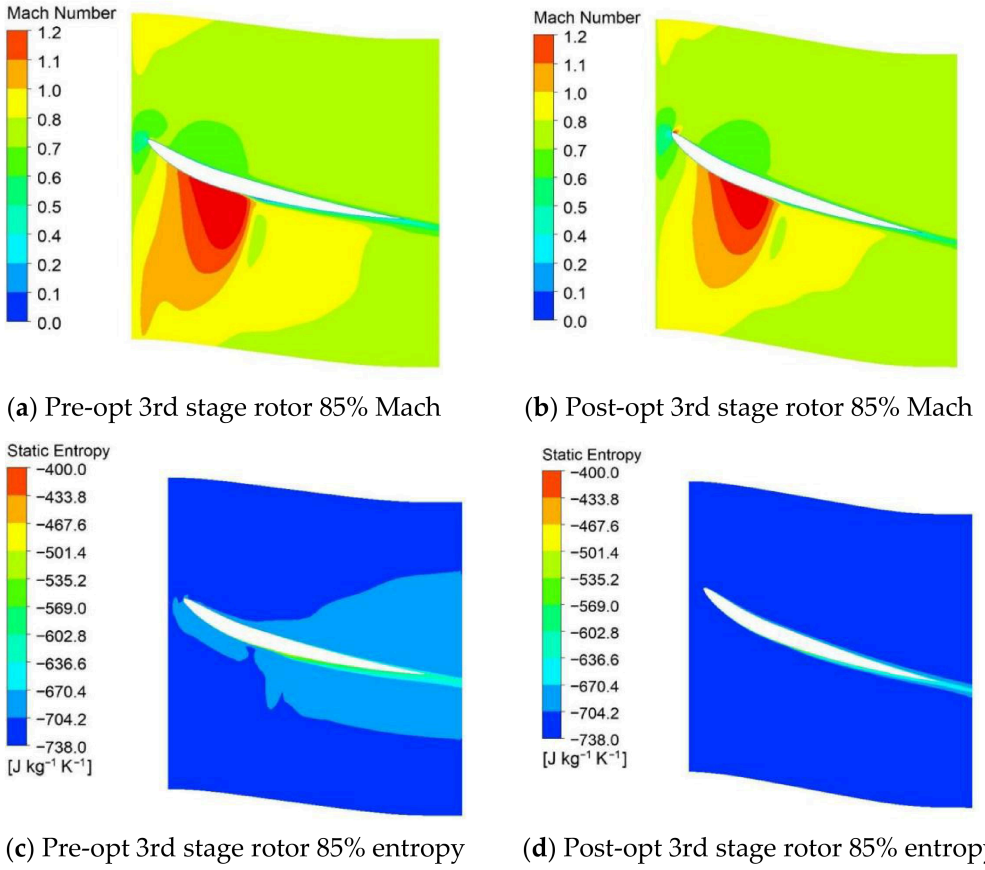


(**a**) Pre-opt 2nd stage stator 85% Mach (**b**) Post-opt 2nd stage stator 85% Mach

(**c**) Pre-opt 2nd stage stator 85% entropy (**d**) Post-opt 2nd stage stator 85% entropy

Figure 9. Comparison of second-stage stator contours before and after optimization.

As shown in the Figure 10a,c, the initial third-stage rotor suffered from strong shock and flow separation problems. A large-area, high-intensity shock was present on the suction side near the leading edge, and separated flow covered most of the suction surface from about 30% of the chord to the trailing edge, reducing the effective flow area and drastically increasing flow losses. As is shown in Figure 10b,d, after optimization, the flow separation area on the suction surface significantly contracted, and the flow separation on the pressure surface was basically suppressed, resulting in a more uniform airflow velocity distribution over the entire blade surface. This indicates that the optimization measures effectively adjusted the aerodynamic load distribution, reducing local flow acceleration and adverse pressure gradients, thereby decreasing the likelihood of boundary-layer separation. Further observation revealed that the streamlines within the optimized blade passage were smoother, corroborating the reduced entropy generation and indicating a substantial improvement in the aerodynamic performance of the third-stage rotor, laying a good foundation for the efficient and stable operation of the entire compressor.



(**a**) Pre-opt 3rd stage rotor 85% Mach (**b**) Post-opt 3rd stage rotor 85% Mach

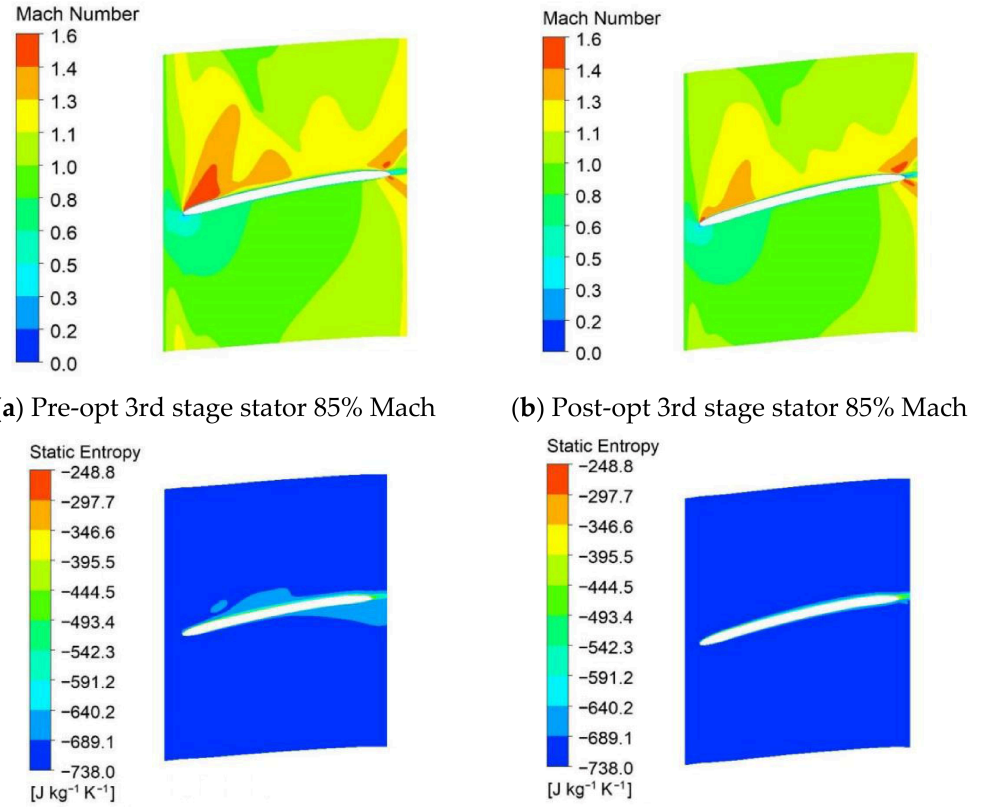
(**c**) Pre-opt 3rd stage rotor 85% entropy (**d**) Post-opt 3rd stage rotor 85% entropy

Figure 10. Comparison of third-stage rotor contours before and after optimization.

As shown in the Figure 11a,c, contour analysis revealed that a significant strong shock existed at the leading edge of the third-stage stator blades, indicating a degree of flow blockage in this region. Additionally, a strong shock and high-Mach-number phenomenon were also present at the trailing edge. Furthermore, a region of high entropy generation was observed in the blade boundary layer. As is shown in Figure 10b,d, after optimization, the high-Mach-number flow region at the leading edge was reduced, and the entropy generation region decreased significantly. The strong shock intensity was noticeably weakened, effectively alleviating the leading-edge flow blockage, and the strong shock phenomenon at the trailing edge essentially disappeared, with the high-Mach-number region substantially reduced. This indicates that the optimization measures, by adjusting the leading-edge shape and trailing edge structure, improved the airflow attachment on the blade surface, and reduced the interaction between the shock and the boundary layer, thereby decreasing local energy losses.

It should be noted that while Mach number and entropy contours provide valuable qualitative comparisons, those based solely on contour visualization are inherently limited. To address this limitation and offer a more rigorous evaluation of the optimization outcomes, the comparative data in Table 4 indicate that the aerodynamic performance of the three-stage stators is significantly improved after closed-loop optimization based on flow field diagnosis. For the first-stage stator, the loss coefficient decreases from 0.1847 to 0.1494, representing a reduction of 19.1%, while the isentropic efficiency increases from 71.83% to 74.24%. For the second-stage stator, the loss coefficient drops from 0.0818 to 0.0765, a decrease of 6.5%, and the efficiency rises from 81.98% to 83.36%. For the third-stage stator, the loss coefficient falls from 0.1205 to 0.1186, with a reduction of 1.6%, and the efficiency increases from 83.02% to 85.04%. In terms of inter-stage distribution, the first stage exhibits the highest loss (0.1494) after optimization, followed by the third stage

(0.1186), and the second stage has the lowest loss (0.0765). This distribution conforms to the typical characteristics of multi-stage axial compressors, namely large shock wave and tip clearance losses in the first stage, moderate endwall secondary flow losses in the last stage, and optimal flow matching in the intermediate stages. Meanwhile, the efficiency increases gradually with the stage number (74.24% → 83.36% → 85.04%), which demonstrates that the flow rectification of the front stages provides a more uniform inlet flow field for the downstream stages. Overall, the adopted optimization measures effectively reduce irreversible flow losses. The improvement in efficiency is highly consistent with the reduction in flow loss, which verifies the effectiveness of the proposed blade profiling and load matching strategy.



(**a**) Pre-opt 3rd stage stator 85% Mach (**b**) Post-opt 3rd stage stator 85% Mach

(**c**) Pre-opt 3rd stage stator 85% entropy (**d**) Post-opt 3rd stage stator 85% entropy]

Figure 11. Comparison of third-stage stator contours before and after optimization.

Table 4. Performance comparison of each stator row before and after optimization.

Stator Row	Loss Coefficient		Efficiency (%)	
	Initial	Optimized	Initial	Optimized
Stator 1	0.1847	0.1494	71.83	75.2350
Stator 2	0.0818	0.0765	81.9764	84.3559
Stator 3	0.1205	0.1186	83.0208	86.0414

3.3. Analysis of Gas Compression Performance Changes

To verify the final performance of the optimized design, numerical simulation of the optimized compressor was conducted, systematically evaluating its gas compression performance. Under a fixed inlet total pressure of 1.33 MPa, for two operating conditions, 60,000 rpm (design speed) and 55,000 rpm (off-design speed), the pressure ratio–mass flow

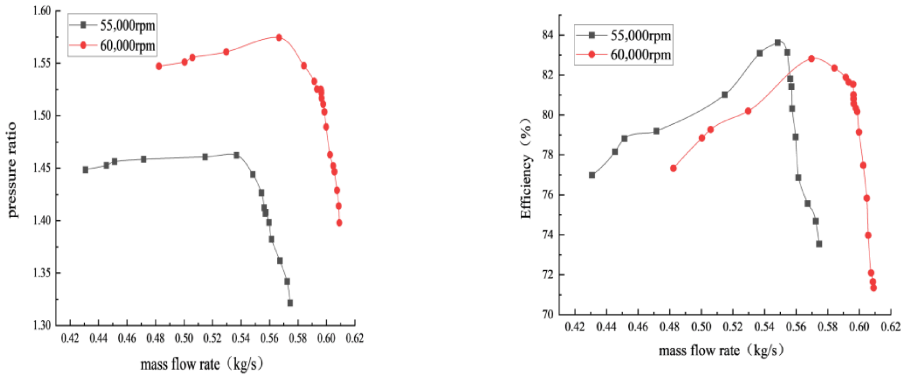
and isentropic efficiency–mass flow characteristic curves were obtained by varying the outlet back pressure (from 0.7 MPa to near-surge conditions), as shown in the figure.

The overall trend shows that as the mass flow rate increases, the pressure ratio gradually decreases, while the isentropic efficiency shows an "inverted U-shaped" distribution, first increasing and then decreasing, representing the compressor's pressure boosting capability and stable operating range. The performance curves for the 60,000 rpm condition are comprehensively superior to those for the 55,000 rpm condition. Key performance parameters are compared in Table 5. The isentropic efficiency values are essentially the same at both speeds, indicating that the rotational speed has minimal impact on the peak energy conversion efficiency. This suggests that the design can achieve nearly optimal efficiency at both speeds, that efficiency optimization is weakly linked to speed, and that the compressor has excellent energy utilization efficiency. The pressure ratio is generally maintained above 1.45, meeting pressurization requirements under small flow rate conditions.

Table 5. Comparison of key compressor performance parameters at different speeds.

Performance Parameter	55,000 (rpm)	60,000 (rpm)	Absolute Change
Surge Point Pressure Ratio	1.45	1.55	0.10
Maximum Pressure Ratio	1.46	1.57	0.11
Choke Mass Flow (kg/s)	0.59	0.64	−0.10
Peak Isentropic Efficiency (%)	83.62	83.63	0.01

Figure 12a shows the mass flow–pressure ratio curves of the compressor at different speeds. Increasing the speed from 55,000 rpm to 60,000 rpm resulted in an overall increase in the pressure ratio. The mass flow–pressure ratio curve for the 55,000 rpm condition initially shows a small rising segment. After the surge point (0.59 kg/s, 1.54), the pressure ratio increases slightly with increasing flow rate. This is because near the surge boundary, some gas stalls due to the high-speed rotation of the blades; a slight increase in flow rate can stabilize the flow path, creating a mild "choking" effect, while increasing the flow rate and velocity through the un-stalled passages, converting dynamic pressure to static pressure and causing a small increase in outlet total pressure until the peak. The pressure ratio then transitions from the peak into a decreasing trend with increasing flow rate. The latter part of the curve shows an almost linear decrease in the pressure ratio with increasing flow rate, due to the continuously increasing negative incidence angle, which reduces the aerodynamic loading and work capacity of the blades. The overall trend of the mass flow–pressure ratio curve at 60,000 rpm is similar to that at 55,000 rpm, both showing an initial increase followed by a decrease in the pressure ratio with increasing flow rate. However, the rising segment is steeper at higher speeds because the higher rotational speed results in a greater impeller circumferential speed, enabling faster energy transfer to the gas. Therefore, when the mass flow increases, the energy per unit mass of gas is higher, leading to a greater increase in pressure ratio with flow rate.



(**a**) Pressure ratio vs. mass flow (**b**) Isentropic efficiency vs. mass flow

Figure 12. Compressor performance curves at different speeds.

Figure 12b shows the mass flow–isentropic efficiency curves of the compressor at different speeds, showing an overall trend of rapid initial rise, reaching a peak, and then declining, with efficiencies all above 76%. Compressor efficiency depends on flow losses during energy conversion, which are closely related to the match between flow rate and rotational speed. At the surge boundary, efficiency is very low. As the flow rate increases, efficiency rises because when the flow rate is below the design condition, the airflow poorly matches the compressor impeller geometry, resulting in low energy conversion efficiency. As the flow rate increases, the flow state gradually approaches the design condition. At 60,000 rpm, the design flow rate of the compressor is larger. When the flow rate increases, the effect of the best efficiency point is more pronounced, the high-efficiency region corresponds to a flow range further to the right, and losses decrease faster; hence, the efficiency rise slope is steeper.

3.4. Analysis of Streamline Evolution and Unsteady Flow Characteristics

To deeply investigate the internal flow mechanisms of the micro-axial compressor during startup and stable operation, this study employed the ANSYS CFX platform with the SST turbulence model to perform high-precision unsteady numerical simulations of the three-stage rotor–stator structure under design conditions (inlet total pressure of 1.33 MPa, total temperature of 365 K, and medium: methane). By extracting and analyzing streamline distributions and flow parameters at six characteristic time points (t = 1 s, 30 s, 90 s, 120 s, 140 s, and 180 s), the dynamic evolution of the internal flow from startup transient to stable operation was systematically revealed.

As shown in Figure 13 (t = 1 s), at the initial startup phase, the rotational speed is low and the airflow has not yet fully developed, resulting in obvious unsteady characteristics of the flow field. Due to the mismatched inflow angle of the airflow at the leading edge of the first-stage rotor blades, local flow separation occurs in the region of 10–20% relative chord length on the suction surface, forming a small-scale separation zone. Intermittent vortices exist in the flow passages of the second-stage and third-stage stator blades, indicating unstable boundary-layer development and failure of the airflow to fully adhere to the blade profiles. At this time, the average airflow velocity is only 14.2 m/s, with significant low-velocity regions in the flow passages leading to large flow losses, and the isentropic efficiency is merely 68.5%.

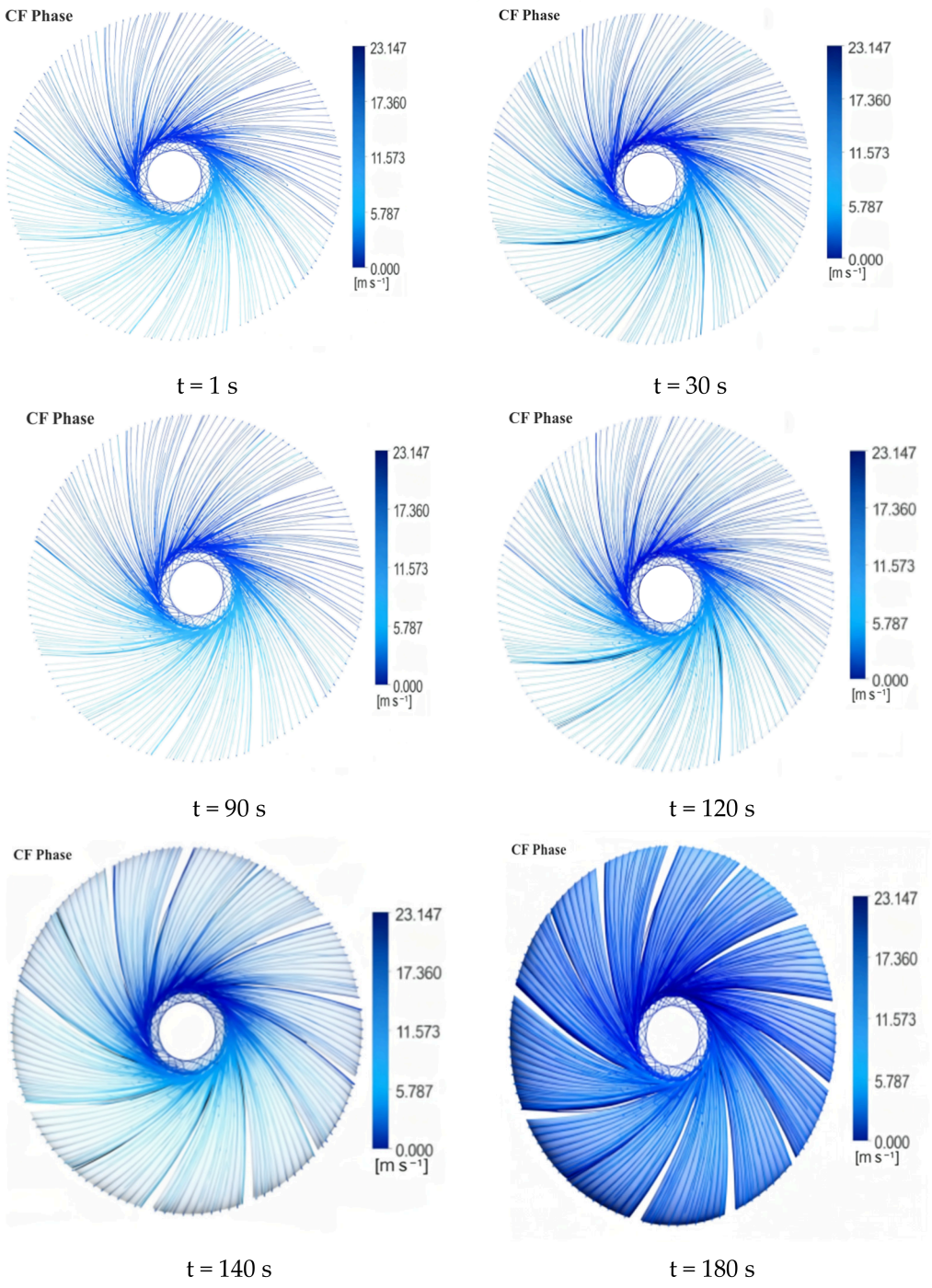


Figure 13. Streamline distributions at different time points.

As shown in Figure 13 (t = 30 s), as the speed increased towards the design value, the flow field gradually stabilized. The leading-edge separation zone on the first-stage rotor completely disappeared, with streamlines smoothly following the blade profile. Vortices in the second-stage stator passage mostly dissipated, and streamline distribution became more uniform. The separation zone on the third-stage rotor suction surface reduced to 5–8% relative chord length. The average flow velocity increased to 62.8 m/s, isentropic efficiency reached 81.7%, and the "C"-shaped structure formed by tip leakage was clear without significant interference to the main flow.

As shown in Figure 13 (t = 90 s–180 s), entering the stable operation phase, the flow field further optimized. By t = 180 s, the leading-edge shock on the first-stage rotor stabilized at the 10% relative chord position, weak and non-diffusing. Streamlines in the

second- and third-stage stator passages were highly parallel, with no separation or vortices. Only a very weak flow mixing zone existed downstream of the third-stage stator trailing edge, not affecting the internal flow. The average flow velocity stabilized at 70.3 m/s, the pressure ratio reached 1.57, and the isentropic efficiency maintained the peak level of 83.6%, indicating that the compressor achieved efficient and stable gas pressurization under design conditions.

3.5. Dynamic Response of Flow Field Parameters and Performance Evolution

To quantify the changes in key aerodynamic parameters during flow field evolution, this study extracted airflow velocity, pressure ratio, isentropic efficiency, and flow characteristic parameters at six time nodes, systematically analyzing the compressor's response mechanism to flow patterns at different operational stages.

As shown in Figure 14 (t = 1 s), during initial startup, due to low speed and high flow inertia, flow separation and secondary flows existed in the flow field, resulting in an average flow velocity of only 14.2 m/s, a pressure ratio of 1.12, and a low isentropic efficiency of 68.5%. Flow losses primarily originated from leading-edge separation and passage vortices.

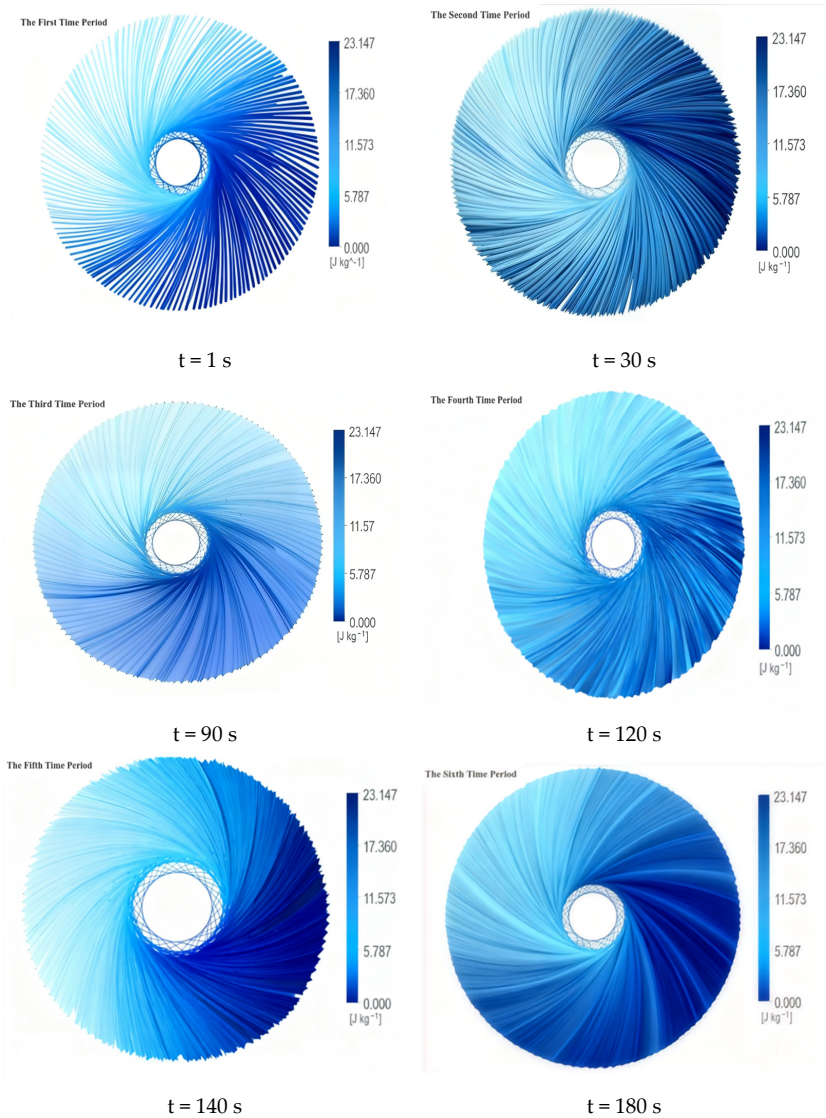


Figure 14. Response to flow patterns at different time points.

As shown in Figure 14 (t = 30 s–120 s), as the speed increased into the design range, the airflow kinetic energy enhanced, boundary-layer development stabilized, and flow separation regions significantly reduced. By t = 120 s, the average flow velocity increased to 65.4 m/s, the pressure ratio improved to 1.51, and isentropic efficiency reached 82.3%. The tip leakage flow formed a stable structure with limited interference to the main flow.

As shown in Figure 14 (t = 140 s–180 s), during the long-term stable operation phase, the flow parameters fully matched the blade geometry, and the flow field reached its optimal state. By t = 180 s, the average flow velocity further increased to 70.3 m/s, the pressure ratio reached 1.57, and isentropic efficiency stabilized at 83.6%. The shock position was fixed and its strength was controllable, with no flow separation phenomena, indicating excellent aerodynamic performance and operational stability of the compressor.

4. Conclusions and Prospects

This research systematically investigated the design and unsteady performance of a micro downhole axial compressor. Through parametric design and flow field diagnostic optimization, combined with high-fidelity unsteady numerical simulations, the following conclusions are drawn.

Optimization design significantly improves aerodynamic performance: Using a flow field diagnostic-based sequential optimization method, targeted adjustments were made to the blade's leading-edge shape, camber line, and thickness distribution, effectively weakening the leading-edge shock strength and suppressing boundary-layer separation. The optimized compressor achieved a pressure ratio of 1.57 and an isentropic efficiency of 83.6% at the design speed, both superior to the initial design targets.

Unsteady flow field reveals stability mechanisms: The flow field undergoes a dynamic evolution from disorder to stability during compressor startup. At t = 1 s, flow separation and passage vortices lead to low efficiency. As speed increases, the flow field gradually homogenizes. By the long-term stable phase at t = 180 s, streamlines fully conform to the blade profile, the shock structure is stable, and no separation occurs, achieving efficient pressurization.

Significant improvement in inter-stage matching and leakage control: The three-stage rotor–stator structure exhibits good inter-stage aerodynamic matching. The tip leakage flow forms a controlled "C"-shaped loop during stable operation without significant interference to the main flow. By optimizing tip clearance and blade loading distribution, leakage losses were further reduced, enhancing operational stability.

Good adaptability to downhole environment: Under simulated real downhole conditions, the compressor demonstrated a wide stable operating range at both rotational speeds, with surge point pressure ratios of 1.45 and 1.55, and choke mass flow rates of 0.59 kg/s and 0.64 kg/s, respectively, meeting the pressurization requirements for low-permeability, low-pressure, and small-flow-rate reservoirs.

Author Contributions: Conceptualization, J.L. and J.Z.; methodology, J.Z.; validation, J.Z.; formal analysis, J.Z.; investigation, J.Z.; resources, J.L.; data curation, J.Z.; writing—original draft preparation, J.Z.; writing—review and editing, J.Z.; visualization, J.Z.; supervision, J.L. All authors have read and agreed to the published version of the manuscript.

Funding: This research received no external funding.

Institutional Review Board Statement: Not applicable.

Informed Consent Statement: Not applicable.

Data Availability Statement: The original contributions presented in this study are included in the article. Further inquiries can be directed to the corresponding author.

Conflicts of Interest: The authors declare no conflicts of interest.

References

1. Nguyen, T.K.; Le, C.H. Thermodynamic analysis of an ejector–vapour compressor cascade refrigeration system. *J. Therm. Anal. Calorim.* **2020**, *141*, 2189–2200. [CrossRef]
2. Wang, Y.; Zhang, J.; Jiang, Z.; Zhou, C.; Liu, W. Investigation on thermodynamic state and valve dynamics of reciprocating compressors with capacity regulation system and parameter optimization. *Eng. Appl. Comput. Fluid Mech.* **2019**, *13*, 923–937. [CrossRef]
3. Liao, Z.; Peng, B.; Zhang, Y.; Zhou, Y.; Yang, X.; Sun, J.; Zhu, B.; Zhang, P. Thermodynamics and performance analysis of a combined algebraic spiral CO_2 scroll compressor. *Appl. Therm. Eng.* **2025**, *279*, 127908. [CrossRef]
4. Guo, Y.; Zhang, S.; Qi, Q.; Peng, X. Study on the thermodynamic performance of the hydraulic-actuated piston compressor by non-destructive methods for hydrogen storage. *Case Stud. Therm. Eng.* **2025**, *74*, 106928. [CrossRef]
5. Song, Y.; Sun, Q.; Yang, S.; Xing, Q.; Cheng, L.; Cao, F. The theoretical and experimental research on the thermodynamic process in transcritical carbon dioxide piston compressor. *Proc. Inst. Mech. Eng. Part E J. Process Mech. Eng.* **2019**, *233*, 267–279. [CrossRef]
6. Staedter, M.A.; Keniar, K.; Garimella, S. Hydrodynamic considerations and design concepts for optimal thermal compressors. *Int. J. Heat Mass Transf.* **2018**, *127*, 209–223. [CrossRef]
7. Wu, S.S.; Wang, J.; Zhang, H.C.; Huang, C.J.; Li, L.F.; Zhou, Y. Thermodynamic analysis of ideal thermocompressor based on Euler view. *IOP Conf. Ser. Mater. Sci. Eng.* **2022**, *1240*, 012035. [CrossRef]
8. Bartnik, R.; Buryn, Z.; Hnydiuk-Stefan, A.; Kowalczyk, T. Thermodynamic and economic comparative analyses of a hierarchic gas-gas combined heat and power (CHP) plant coupled with a compressor heat pump. *Energy* **2022**, *244*, 123116. [CrossRef]
9. Neumeier, Y.; Mishra, A.; Prasad, J.V.; James, D.K. Modeling and Simulation of Unsteady Flow in Multistage Compressors Using Interdomain Boundaries. *J. Propuls. Power* **2022**, *38*, 494–507. [CrossRef]
10. Grieb, M.; Brümmer, A. Thermodynamic simulation of a water-injected twin-screw steam compressor. *IOP Conf. Ser. Mater. Sci. Eng.* **2024**, *1322*, 012017. [CrossRef]
11. Zhao, Z.; Wang, G.; He, J.; Tian, Y. Thermodynamics and dynamic investigation of ultra-high-pressure diaphragm compressor. *Front. Energy Res.* **2024**, *12*, 1365558. [CrossRef]
12. Yang, L.; Jia, X.; Peng, X. Analysis of the Thermodynamic Characteristics of a Hyper-Compressor through Numerical Simulation and Experimental Investigation. *Appl. Sci.* **2023**, *13*, 4478. [CrossRef]
13. Gao, X.; Liu, Y. Thermodynamic analysis of a novel self-air-cooling reciprocating compressor. *IEEE Access* **2021**, *9*, 79225–79235. [CrossRef]
14. Rusanov, A.V.; Solovey, V.V.; Lototskyy, M.V. Thermodynamic features of metal hydride thermal sorption compressors and perspectives of their application in hydrogen liquefaction systems. *J. Phys. Energy* **2020**, *2*, 021007. [CrossRef]
15. Li, X.; Wang, X.; Zhang, Y.; Fang, L.; Deng, N.; Zhang, Y.; Jin, Z.; Yu, X.; Yao, S. Experimental and economic analysis with a novel ejector-based detection system for thermodynamic measurement of compressors. *Appl. Energy* **2020**, *261*, 114395. [CrossRef]
16. Li, Z.; Liang, K.; Jiang, H. Thermodynamic analysis of linear compressor using R1234yf. *Int. J. Refrig.* **2019**, *104*, 530–539. [CrossRef]
17. Zhao, B.; Zhou, S.; Feng, J.; Peng, X.; Jia, X. Application of a Fluid-Structure Interaction Model for Analysis of the Thermodynamic Process and Performance of Boil-Off Gas Compressors. *Entropy* **2019**, *21*, 341. [CrossRef] [PubMed]
18. Sharma, V.K.; Kumar, E.A. Thermodynamic Analysis of Two Stage Metal Hydride Based Hydrogen Compressor. *Mater. Today Proc.* **2018**, *5*, 23218–23223. [CrossRef]
19. Ma, S.-B.; Choi, J.; Shim, H.-S. Impact of Surface Roughness on Aerodynamic Performance of Axial Compressor Blades under Various Altitude Conditions. *Aerosp. Sci. Technol.* **2025**, *164*, 110368. [CrossRef]
20. Zhang, B.; Liu, B.; Mao, X.; Wu, X.; Wang, H. Effect of hub clearance size and shape of a cantilevered stator on the performance of a small-scale transonic axial compressor. *Proc. Inst. Mech. Eng. Part A J. Power Energy* **2022**, *236*, 609–620. [CrossRef]
21. Pinelli, L.; Burberi, C.; Ignesti, M.; Michelassi, V.; Tapinassi, L.; Abati, A.; Pacciani, R. Forced response in a multi-stage aeroderivative axial compressor with acoustic excitations: Method validation with field data. *Aerosp. Sci. Technol.* **2023**, *138*, 108305. [CrossRef]
22. Cai, J.; Wu, Y.; Wang, Y.; Chen, B.; Qu, X.; Wen, H. Design passive magnetic mechanisms with modular magnet configuration for axial gas force balance in miniature scroll compressors. *Int. J. Refrig.* **2024**, *166*, 42–52. [CrossRef]
23. Li, J.; Du, J.; Nan, X.; Liu, L.; Lin, F. Coupling stability-enhancing mechanism with compact self-recirculating injection in an axial flow compressor. *Proc. Inst. Mech. Eng. Part A-J. Power Energy* **2016**, *230*, 696–708. [CrossRef]

24. Yokoyama, H.; Minowa, K.; Orito, K.; Nishikawara, M.; Yanada, H. Compressible Simulation of Flow and Sound Around a Small Axial-Flow Fan With Flow Through Casing Slits. *J. Fluids Eng.* **2020**, *142*, 101215. [CrossRef]
25. Kim, S.; Im, J.H.; Ryu, G. A study on one-dimensional model correction for axial-flow compressors based on measurement data. *Aerosp. Sci. Technol.* **2023**, *133*, 108139. [CrossRef]

Disclaimer/Publisher's Note: The statements, opinions and data contained in all publications are solely those of the individual author(s) and contributor(s) and not of MDPI and/or the editor(s). MDPI and/or the editor(s) disclaim responsibility for any injury to people or property resulting from any ideas, methods, instructions or products referred to in the content.